Energy Conversion and Management 198 (2019) 111929

Contents lists available at ScienceDirect

Energy Conversion and Management

journal homepage: www.elsevier.com/locate/enconman

Adaptive model predictive control for hybrid energy storage energy management in all-electric ship microgrids

Jun Hou[a], Ziyou Song[b,*], Heath Hofmann[a], Jing Sun[a,b]

[a] Department of Electrical Engineering and Computer Science, University of Michigan, Ann Arbor, Michigan 48109, USA
[b] Department of Naval Architecture and Marine Engineering, University of Michigan, Ann Arbor, Michigan 48109, USA

ARTICLE INFO

Keywords:
All-electric ships
Energy management
Adaptive model predictive control
Parameter uncertainties
Hybrid energy storage

ABSTRACT

Hybrid energy storage systems have been widely used in transportation, microgrid and renewable energy applications to improve system efficiency and enhance reliability. However, parameter uncertainty can significantly affect system performance. In order to address this issue, an adaptive model predictive control is developed in this paper. Online parameter identification is used to mitigate parameter uncertainty, and model predictive control is used to optimally split power, deal with constraints, and achieve desired dynamic responses. A sensitivity analysis is conducted to identify major impact factors. In order to validate the proposed method, both simulation and experiments are performed to show the effectiveness of the proposed adaptive model predictive control. Compared to the model predictive control without online parameter identification, the power loss reduction can be as high as 15% in the experiments. This study focuses on all-electric ship energy management to mitigate load fluctuations and improve system efficiency and reliability. The proposed method could also be used in other applications.

1. Introduction

Hybrid energy storage systems (HESSs) combine different energy storage devices (ESDs) to leverage their complementary characteristics for efficient and effective system solutions [1]. In [2], an HESS that consists of a battery and a fuel cell for application in electric buses has been studied. In [3], an HESS consisting of a battery, an ultracapacitor, and a fuel cell was used to improve fuel economy and system performance. Battery with ultra-capacitor (UC) is one of the most widely used HESSs. An HESS with battery and UC has been explored in renewable energy applications [4], microgrid applications [5], hybrid electric vehicles [6], fuel cell electric vehicles [7], and all-electric ships [8]. As an electrochemical device, batteries have high energy density but low power density, while UCs store energy in an electric field, leading to higher power density, but lower energy density. Furthermore, compared to UCs, the main limitations of batteries are their relatively short cycle life and limited recharge rate [9]. As a battery's capacity degrades, its internal resistance increases significantly, resulting in increased losses [10]. Moreover, batteries are more sensitive to temperature. Only a narrow temperature range of operation (15 °C–35 °C) is recommended, outside of which battery capacity drops significantly at low temperatures (especially lower than 0 °C), and can have irreversible degradation at high temperatures [11]. Safety issues have also been identified at high operating temperatures, particularly for Li-ion batteries. UC has a relatively long cycle life, typically over 1 million cycles [12]. Furthermore, UC has fast dynamic response to support pulse or high-frequency power loads [13]. UC is less sensitive to temperature and has a smaller internal resistance to provide more efficient operation [14]. In general, battery is preferred for a long-duration load thanks to its high energy density, whereas UC is more suitable for a short-duration high-power load. The combination of battery and UC can therefore provide complementary characteristics in terms of improved efficiency, enhanced cycle life, and reduced size, weight and cost. However, the effectiveness of HESS relies on energy management strategies.

Energy management strategies aim to coordinate multiple power sources and loads in order to achieve efficient and reliable operation and to meet various dynamic requirements. Model predictive control (MPC) technology has been found to be an effective energy management strategy in a wide variety of application areas, such as smart buildings, automotive, and microgrids. In [15], a real-time building energy simulation method is developed for MPC to improve the system performance. Literature [16] has developed a two-level MPC to reduce the costs in home appliances with good thermal regulation performance. A nonlinear model predictive control strategy is developed in [17] to improve the fuel economy of hybrid electric buses. In [18], a model predictive control strategy is developed for a plug-in hybrid

* Corresponding author.
E-mail addresses: junhou@umich.edu (J. Hou), ziyou@umich.edu (Z. Song), hofmann@umich.edu (H. Hofmann), jingsun@umich.edu (J. Sun).

https://doi.org/10.1016/j.enconman.2019.111929
Received 6 May 2019; Received in revised form 7 August 2019; Accepted 9 August 2019
Available online 18 August 2019
0196-8904/

electric vehicle with a battery/UC HESS. A hybrid photovoltaic-wind-diesel-battery system using MPC has been studied in [19]. The advantage of MPC is that it can provide an optimal solution within a predictive horizon, deal with constraints, and take system dynamics into consideration [20].

In this paper, the energy management of all-electric ships is studied. All-electric ships have become a dominant trend for both commercial and military ship development to improve efficiency, support high-power mission systems, reduce emissions, and provide a more comfortable environment [21]. Propulsion-load fluctuations have multi-frequency characteristics, which are caused by wave effects (resulting in low-frequency fluctuations) and propeller rotation (resulting in high-frequency fluctuations) [8]. HESS has been explored to address propulsion-load fluctuations on the shipboard microgrid, since using only one single type of ESD can result in increased size, weight, and cost [22]. Energy management strategies using MPC on shipboard microgrids have been investigated in the literature [23]. In [24], a nonlinear MPC is developed to compensate pulse power loads and track references, including the desired bus voltage, desired reference power for generator sets, and desired reference speed for the motor. In [25], a stochastic MPC is developed to smooth out power fluctuations. A scenario-based economic model predictive control is developed for marine electric power plants in [26]. The authors in [27] have developed an energy management scheme based on MPC to optimize the power balance between distributed resources and load devices. In [28], MPC is used to optimize the active power filter operation in a shipboard network. An MPC-based predictive energy management is developed in [29] to improve the fuel efficiency of all-electric autonomous ships. In [30], MPC is used for the dynamic optimization of ship energy efficiency. However, the literatures aforementioned do not consider parameter uncertainty, especially HESS parameters. To the best of the authors' knowledge, the impact of HESS parameter uncertainty has not been well explored, and there is no existing literature that quantitatively discusses the sensitivity of HESS parameter uncertainties to the performance. For example, the internal resistance of a battery can be significantly increased as the temperature drops or the battery degrades. Even at constant temperature, the internal resistance can vary with SOC, and the variation can be over 100% [31]. This parameter variation could significantly affect the performance of MPC, leading to increased losses and power tracking errors.

In order to deal with the issue of HESS parameter uncertainty, an adaptive MPC energy management strategy, which combines online parameter identification and MPC, is developed in this paper. The equivalent circuit model (ECM) is used as the optimization-oriented HESS model. A detailed HESS dynamic model can capture system dynamics more accurately at the cost of increased computational complexity, leading to major challenges in real-time applications; while, a simplified model is preferred for real-time application, but an over-simplified model cannot capture key dynamics. It is therefore essential to develop a suitable model for a specified application. According to the propulsion-load characteristics, an analysis is performed to determine how to choose the appropriate HESS model. A sensitivity analysis is performed to study the impact of HESS parameter uncertainty on MPC. In this study, major impact factors are identified. These factors determine how sensitive of HESS to its parameter uncertainties when constraints are inactive. Detailed simulation case studies are performed to validate the analysis and provide additional insights into the impact of HESS parameter uncertainties when constraints are active. In order to evaluate the proposed adaptive MPC and sensitivity analysis, experimental studies are performed on a physical testbed. The adaptive MPC and MPC without online parameter identification are compared to demonstrate the effectiveness of the proposed energy management strategy. Moreover, the sensitivity analysis is also validated by experimental results.

In the authors' previous work, the modeling of propulsion-load fluctuations has been developed in [32]. The work in [8] mainly provides insights into the comparison between batteries/flywheels HESS and batteries/UCs HESS. In [33], the major effort focuses on the implementation and evaluation of a proposed real-time MPC for both pulse-power load and propulsion-load fluctuations. None of them deals with the issue of HESS parameter uncertainties. The major contributions of this paper are summarized in the following:

- An adaptive MPC energy management strategy is developed to optimize system performance and address the issue of HESS parameter uncertainty.
- A sensitivity analysis is studied to provide an analytical estimation of the impact on HESS parameter uncertainties.
- An experiment is performed to evaluate the proposed energy management strategy as well as the sensitivity analysis.

This paper is organized as follows. The modeling of propulsion-load fluctuations on a shipboard network is presented in Section 2. In Section 3, an optimization-oriented model is discussed and developed. The adaptive MPC is developed in Section 4. Section 5 presents a sensitivity analysis that determines the impact of HESS parameter uncertainty on the MPC. Experimental results are presented in Section 6. Section 7 concludes the paper.

2. Propulsion-load power fluctuations on a shipboard network

The propulsion-load model developed in [32] is used for this study, where the key elements of the model are presented for easy reference.

The total propulsion-load power can be expressed as:

$$P_{Load} = 2\pi n T_{Load}, \tag{1}$$

where n is the propeller rotational speed (in revolutions-per second) and T_{Load} is the load torque generated by the propeller. In this study, no gear box is used between the motor and propeller, so that n is also the motor rotational speed. The load torque can be expressed as [33]:

$$T_{Load} = \mathrm{sgn}(n)\beta K_{Q0}\rho n^2 D_P^5, \tag{2}$$

where β presents the loss factor to capture the propeller in-and-out-of-water impact, ρ is the water density, and K_{Q0} and D_P are the torque coefficient and the diameter of the propeller, respectively. The torque coefficient K_{Q0} is a function of the ship advance speed V_a, which can be represented by wake field $w = \frac{U - V_a}{U}$ and ship speed U. The mathematical equation is presented as follows [33]:

$$K_{Q0} = f_{K_Q}\left(J_A,\ Pitch/D_P,\ A_e/A_o,\ Z,\ R_n\right), \tag{3}$$

where $J_A = \frac{V_a}{nD_P}$ is the advance coefficient, $Pitch/D_P$ and A_e/A_0 are the pitch ratio and the expanded blade-area ratio, respectively, and Z and R_n are the blade number and the Reynolds number, respectively.

High-frequency fluctuations are caused by the wake field w, and the wave effect results in low-frequency fluctuations through the ship speed U and the in-and-out-of-water behavior (which is captured by β). The ship speed is given by:

$$\left(m + m_x\right)\frac{dU}{dt} = T_{thrust}\left(1 - t_d\right) + R + F, \tag{4}$$

where m and m_x are the mass and added-mass of the ship, respectively, T_{thrust} is the thrust generated by the propeller, t_d represents the thrust deduction coefficient, F represents wave disturbances, and R is the total resistance force, which includes frictional, wave-making and wind resistances.

The propulsion-load power fluctuation P_{FL} is obtained by:

$$P_{FL}(k) = P_{Load}(k) - P_{Avg}(k), \tag{5}$$

where P_{Avg} is the average value of P_{Load}. The average power P_{Avg} is calculated by:

Table 1
Ship parameters.

Description	Parameter	Value
Ship length	L_{ship}	190 m
Ship breadth	B_{ship}	28.4 m
Draft	H	15.8 m
Mass	m	20000 ton
Added-mass	m_x	28755 ton
Thrust deduction coefficient	t_d	0.2
Propeller diameter	D_P	5.6 m
Wetted area	S	12297 m^2
Advance facing area in the air	A_T	675.2 m^2
Water resistance coefficients	$C_F + C_R$	0.0043
Air resistance coefficient	C_{air}	0.8

$$P_{Avg}(k) = \frac{\sum_{k=t-T_{wave}}^{t} \left(P_{Load}(k)\right)}{T_{wave}}, \tag{6}$$

where T_{wave} is the wave period. For this study, an electric cargo ship is used as an example, whose key parameters are shown in Table 1[33]. Three different sea states (SS), corresponding to smooth (SS2), moderate (SS4), and severe (SS6) operating conditions, respectively, are used in the simulation and analysis. Parameters associated with wave behavior and operating conditions are shown in Table 2. The load power fluctuations at both SS4 and SS6 are shown in Fig. 1, where the time trace of power fluctuations, as well as their frequency spectrums, are clearly presented.

3. Optimization-oriented hybrid energy storage system model

The equivalent circuit model (ECM) is one of the effective models to achieve reliable battery state estimation [34]. The first-order RC ECM has been widely used in many applications, especially for system-level energy management strategy development. The first-order RC ECM is shown in Fig. 2, where an ohmic resistor with resistance R_s, a parallel RC network ($R_t//C_t$), and a DC source with voltage V_{OC} are connected in series [35].

The battery terminal voltage and current are defined as V_B and I_B respectively (positive I_B for discharge and negative I_B for charge). Four parameters, including R_s, R_t, τ (i.e., $R_t C_t$), and V_{OC}, should be identified simultaneously to guarantee the model accuracy [36]. The parametric model of the first-order RC ECM can be expressed as:

$$\dot{V}_B = \theta_B^T X_B, \tag{7}$$

where

$$\theta_B = \left[R_s \frac{R_t + R_s}{\tau} \frac{1}{\tau} \frac{V_{OC}}{\tau}\right]^T, X_B = [-\overline{I}_B - I_B - V_B 1]^T,$$

where v_C is the voltage across the RC network, V_{OC} and R_s are functions of battery SOC and their variations with respect to time are much smaller than that of v_C[37], θ_B is the parameter vector to be identified, and X_b is the information vector which can be obtained through measurement and calculation. In the parameter identification, X_b should be persistently exciting (PE) to ensure parameter convergence regardless

Table 2
Parameters for simulation study.

Description	Parameter	Value
Wave period	T_{wave}	12 s
Wave height	h_{wave}	0.5 m(SS2)/ 2 m(SS4)/ 4 m(SS6)
Wave length	L_{wave}	40.29%L_{ship}
Ship speed command	U_d	12.4 knot
Motor speed command	ω_d	125 rpm

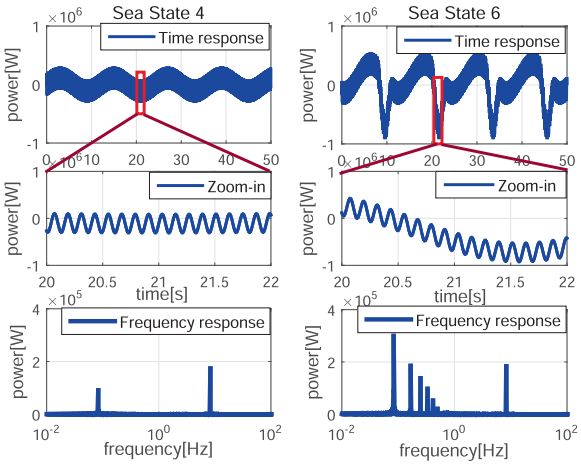

Fig. 1. Load power fluctuations (top plots), zoom-in fluctuations (middle plots), and their frequency spectrums (bottom plots) [33].

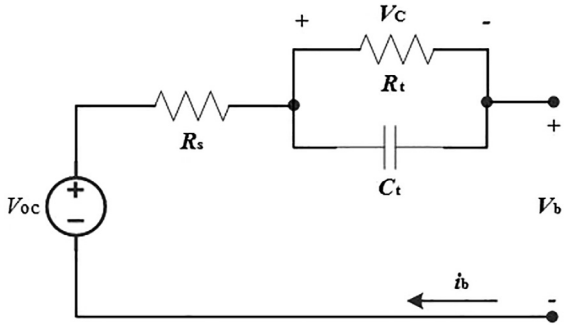

Fig. 2. The first-order RC equivalent circuit model for the battery.

of the algorithm used [38]. To guarantee parameter convergence, at least two frequency components should be included in X_b.

The Recursive Least Squares (RLS) with a constant forgetting factor of 0.992 is used to identify the parameters of the battery pack [39]. As shown in Fig. 3, the ohmic resistance R_s is about 60 mΩ, and R_t is about 187 mΩ. The battery pack time constant τ is about 60s.

Based on the identified parameters, the terminal voltage can be estimated accordingly. As shown in Fig. 4, the estimated terminal voltage can accurately track the measured voltage, and the estimation error is below 0.5%.

The experimental results show that the first-order RC ECM can

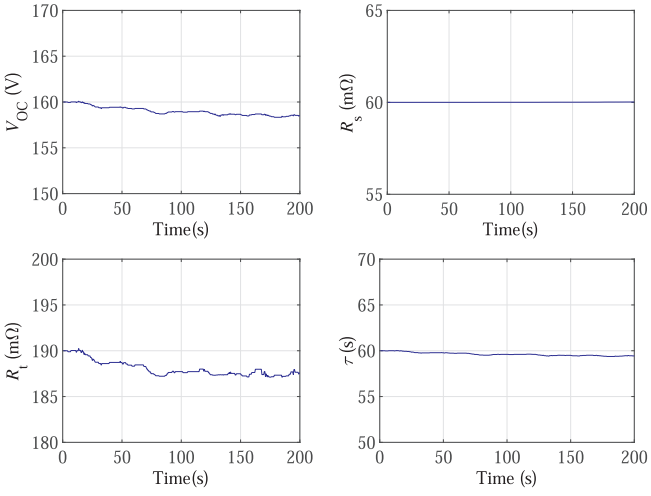

Fig. 3. Parameter identification results of the battery pack in an experiment.

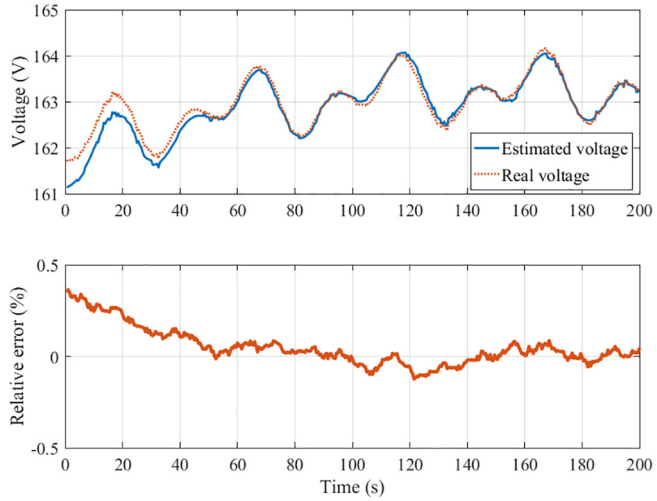

Fig. 4. Terminal voltage estimation results in an experiment.

accurately represent the battery dynamics. However, the first-order RC ECM for battery will increase the states in the proposed MPC, and therefore significantly increase the computational cost, which may hinder the online application of MPC. The control and prediction horizons of the proposed MPC are 0.02 s and 0.4 s respectively, and the time constant τ is about 60 s. Therefore, in the MPC control process, which has a much shorter period than the battery time constant, the RC network can be considered as a short circuit. The instantaneous power loss for the prediction horizon of MPC is mainly determined by V_{OC} and R_s but not the RC pair, because the time constant of the RC pair is much higher. Since the battery pack has slow dynamics, the battery ECM can be simplified without the RC pair to estimate the battery power loss over the prediction horizon. Moreover, only V_{OC} and an equivalent series resistance R_B need to be identified. For the UC, the equivalent series resistance R_{UC} is used for its ECM.

Therefore, the HESS model is presented as follows:

$$\dot{SOC}_B=\frac{-I_B}{3600Q_B},\dot{SOC}_{UC}=\frac{-I_{UC}}{V_{max}C_{UC}}, \tag{8}$$

where SOC_B and SOC_{UC} are the SOCs of battery and UC, respectively, I_B and I_{UC} are the battery current and UC current, respectively, Q_B represents the battery capacity (in Ah), V_{max} and C_{UC} are the maximum voltage and the capacitance of the ultra-capacitor, respectively. The terminal powers of the HESS are obtained as follows:

$$P_B = N_B(V_{OC}I_B - R_BI_B^2),P_{UC} = N_{UC}(V_{max}SOC_{UC}I_{UC} - R_{UC}I_{UC}^2), \tag{9}$$

where N_B and N_{UC} are the module numbers of battery and UC in the HESS, respectively.

4. Adaptive model predictive control

In order to mitigate power fluctuations with high efficiency, an adaptive MPC is developed in this section. In the cost function of MPC, three terms are considered. The first one is to minimize the power compensation error. The output power of battery and UC are used to compensate the fluctuation power P_{FL}. The second term is to reduce HESS losses and optimize the HESS efficiency. In order to address the limitation of a short predictive horizon [32], an additional SOC reference term $((SOC_{UC}(k) - SOC_{UC_{ref}})^2)$ is included as the third term in the cost function. Knowledge of HESS parameters is essential for optimizing system operation. HESS parameter uncertainties could lead to significant energy losses. In order to address this issue, an indirect adaptive control is combined with the receding horizon MPC, leading to the proposed adaptive MPC. The control diagram is shown in Fig. 5, and the adaptive MPC is expressed as follows:

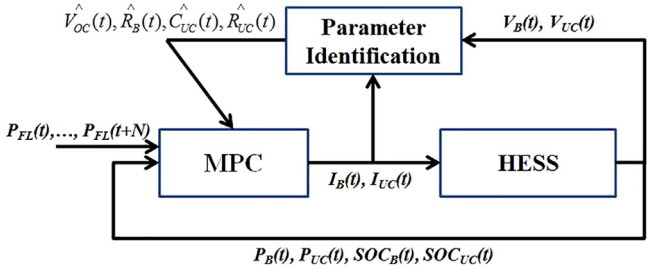

Fig. 5. Control Diagram of the adaptive MPC energy management strategy.

$$\begin{aligned}\min: J=&\sum_{k=t+1}^{t+N}\left[\lambda_{Tracking}(P_{FL}(k)-\hat{P}_B(k)-\hat{P}_{UC}(k))^2\right]\\&+\sum_{k=t}^{t+N}\left[\lambda_{Loss}\left(N_B\hat{R}_BI_B^2(k)+N_{UC}\hat{R}_{UC}I_{UC}^2(k)\right)\right]\\&+\sum_{k=t}^{t+N}\left[\gamma_{UCSOC}\left(SOC_{UC}(k)-SOC_{UC_{ref}}\right)^2\right]\\&+\lambda_{Tracking}(P_{FL}(t)-P_B(t)-P_{UC}(t))^2,\end{aligned} \tag{10}$$

subject to the constraints:

$$\begin{bmatrix}SOC_B(k+1)\\SOC_{UC}(k+1)\end{bmatrix}=\begin{bmatrix}SOC_B(k)\\SOC_{UC}(k)\end{bmatrix}-\begin{bmatrix}\frac{T_s}{3600Q_B}&0\\0&\frac{T_s}{V_{max}\hat{C}_{UC}}\end{bmatrix}\begin{bmatrix}I_B(k)\\I_{UC}(k)\end{bmatrix}, \tag{11}$$

$$SOC_{minB}\leqslant SOC_B\leqslant SOC_{maxB}, \tag{12}$$

$$SOC_{minUC}\leqslant SOC_{UC}\leqslant SOC_{maxUC}, \tag{13}$$

$$I_{minB}\leqslant I_B\leqslant I_{maxB}, \tag{14}$$

$$I_{minUC}\leqslant I_{UC}\leqslant I_{maxUC}, \tag{15}$$

where N is the predictive horizon, T_s is the sampling time, λ and γ are the weighting factors to put different emphasis on each attribute, $\hat{R}_B$ and $\hat{R}_{UC}$ are the internal resistances of the battery and UC from online parameter identification, respectively, $\hat{C}_{UC}$ is the estimated UC capacitance, SOC_{minB} (SOC_{maxB}) and SOC_{minUC} (SOC_{maxUC}) are the lower (upper) boundaries of the SOC of the battery and UC, respectively, and I_{minB} (I_{maxB}) and I_{minUC} (I_{maxUC}) are the lower (upper) boundaries of the output currents of the battery and UC, respectively. In (10), the objective of this cost function is to minimize the power tracking error (power fluctuation mitigation), HESS energy losses (efficiency improvement), and the variation of UC from its reference state (SOC planning). The system dynamic is captured by (11), and Eqs. (12)–(15) represent the physical constraints of the battery and UC. Note that $P_B(t)$ and $P_{UC}(t)$ are the instantaneous output power from the measurement, while $\hat{P}_B(k)$ and $\hat{P}_{UC}(k)$ are the predictive output power from the online estimation for $k = t + 1, ..., t + N$. In the parameter identification, the variations of V_{OC} and C_{UC} are much smaller than R_B and R_{UC}. The internal resistance of HESS, especially R_B, can significantly change with SOC, temperature and cycle life, and the variation can be more than 100%. Furthermore, they can directly affect the MPC for splitting power between batteries and UCs. It is very important to understand the impact of HESS internal resistances. Therefore, a sensitivity analysis is performed in the section.

5. Sensitivity analysis

In order to provide insights into the impact of HESS parameter uncertainties, a sensitivity analysis is performed. The main objective of this analysis is to determine major impact factors, which might be load power, battery and UC voltages, and numbers of battery and UC modules. The major factors determine how sensitive of a given HESS to its parameter uncertainties and how significant to the MPC performance.

After that, a more realistic case study is performed to validate the analysis and provide insights into additional impacts, which cannot be provided by the analysis.

5.1. Major factor analysis

An analysis is conducted to determine the impact of HESS parameters. Several assumptions are made for this analysis:

- the HESS constraints in (12)–(15) are inactive;
- the power fluctuations are fully compensated ($P_{FL} = P_B + P_{UC}$);
- a one-step predictive horizon is considered ($N = 1$);
- the terminal voltages of battery (V_B) and UC (V_{UC}) are slow-time varying, leading to $V_B(k) \approx V_B(k-1)$ and $V_{UC}(k) \approx V_{UC}(k-1)$.

Note that the impacts when the assumption is not valid, such as the constraints are active, will be discussed in the next section. According to the assumption, the cost function can be simplified as:

$$J\left(I_B(k), I_{UC}(k)\right) = \alpha I_B^2(k) + \frac{(P_{FL}(k) - N_B V_B(k) I_B(k))^2}{N_{UC}^2 V_{UC}^2(k)}. \tag{16}$$

Since the HESS does not reach its constraints, the optimal solutions of (16) can be presented as:

$$\begin{aligned} I_B(k) &= \frac{P_{FL}(k) N_B V_B(k)}{\alpha (N_{UC} V_{UC}(k))^2 + (N_B V_B(k))^2}, I_{UC}(k) \\ &= \frac{\alpha P_{FL}(k) N_{UC} V_{UC}(k)}{\alpha (N_{UC} V_{UC}(k))^2 + (N_B V_B(k))^2}. \end{aligned} \tag{17}$$

The total HESS loss is given by:

$$Loss_{HESS}(k) = \frac{\alpha N_{UC} R_{UC} P_{FL}^2(k)}{\alpha (N_{UC} V_{UC}(k))^2 + (N_B V_B(k))^2}. \tag{18}$$

If the HESS parameters are not correct, the internal resistance ratio α becomes α'. The total HESS loss calculated by incorrect parameters:

$$Loss'_{HESS}(k) = \frac{N_{UC} R_{UC} P_{FL}^2(k)(\alpha N_B^2 V_B^2(k) + (\alpha' (N_{UC} V_{UC}(k))^2)}{(\alpha' (N_{UC} V_{UC}(k))^2 + (N_B V_B(k))^2)^2}. \tag{19}$$

In order to evaluate the benefits of using correct parameters, the performance matric is defined as:

$$Loss_{diff}\% = \frac{Loss'_{HESS} - Loss_{HESS}}{Loss_{HESS}} \times 100\%; \tag{20}$$

Take (18) and (19) into (20), then the improvement of HESS losses can be presented as:

$$Loss_{diff}\% = \frac{(\alpha - \alpha')^2 \nu^2}{\alpha (\alpha' + \nu^2)^2} \times 100\% = \frac{\alpha (1-n)^2 \nu^2}{(n\alpha + \nu^2)^2} \times 100\%, \tag{21}$$

where ν is defined as the voltage ratio $\frac{N_B V_B}{N_{UC} V_{UC}}$ and $n = \frac{\alpha'}{\alpha}$.

Remark 5.1 (Major impact factors): Even though this is a simplified case study, it provides very important insights into the impact of parameter uncertainties. According to this analysis, the major impact factors are the voltage ratio ν and the internal resistance ratio α. The load power has little impact on the control performance. However, when the load power is large enough to force the HESS to operate at its physical constraints over a long time, then the impact of load power is significant. Therefore, the analysis in Eq. (21) is valid when the HESS is not operating at its constraints.

5.2. Simulation case study

Two cases, which have two different voltage ratios ν and the internal resistance ratios α, are considered in this study. The HESS information of each case is shown in Table 3. In this section, the results at SS2 are presented and analyzed first. Due to relatively small load fluctuations at SS2, the constraints in (12)–(15) are inactive. As follows, the load fluctuations at SS4 are studied. At SS4, the UC reaches its current constraints. The inequality constraint of UC current, however, is only active over a short duration, and the HESS is still able to fully compensate the load fluctuations. The results at SS6 are discussed in the sequel. At SS6, the constraints are active over a long duration, and the battery and UC cannot compensate all of the fluctuations.

Table 3
HESS configuration and size selection.

	Case 1	Case 2
Battery (N_B)	8 modules	6 modules
Ultra-capacitor (N_{UC})	8 modules	9 modules
Internal resistance of one battery module (R_B)	64 mΩ	64 mΩ
Internal resistance of one UC module (R_{UC})	18 mΩ	8.6 mΩ
Open-circuit voltage of one battery module (V_{OC})	128 V	128 V
Capacitance of one UC module (C_{UC})	63 F	63 F
Maximum voltage of one UC module (V_{max})	125 V	125 V

5.2.1. Sea state 2: inequality constraints are inactive

Due to the smooth encountered wave, the propulsion-load fluctuations at SS2 are relatively small. The HESS can fully compensate the fluctuations without reaching its physical constraints. In order to evaluate the analysis in Section 5.1, the performance of HESS losses is studied in a 12 s duration first, which is one wave period. The voltage drop of the UC is ignorable in this 12 s and therefore $\gamma_{UC_{SOC}} = 0$. In order to achieve no tracking error, the weighting factor $\lambda_{Tracking}$ must be much larger than λ_{Loss} because of the competition between "power tracking" and "HESS losses", in the sense that reducing the tracking error would lead to increased HESS losses, and vice versa. However, a numerical problem could happen when $\lambda_{Tracking} \gg \lambda_{Loss}$. For example, when $\lambda_{Tracking} \approx 1$ and λ_{Loss} is close to 0, such as 10^{-9}, then the HESS losses cannot be taken into consideration, resulting in the non-optimal power split between the battery and UC. Therefore, the cost function in Eq. (10) is modified as follows:

$$J = \sum_{k=t}^{t+N} \left(N_B R_B I_B^2(k) + N_{UC} R_{UC} I_{UC}^2(k) \right), \tag{22}$$

subject to

$$P_{FL}(k) = P_B(k) + P_{UC}(k), \tag{23}$$

and the constraints in Eqs. (11)–(15).

In order to evaluate the impact of the HESS parameter uncertainties, six simulations of each case are performed. The battery and UC internal resistances without online parameter identification are defined as R'_B and R'_{UC}, respectively. The HESS internal resistance could change over 100% at different temperatures, SOCs, and health conditions. For example, literature [40] shows the charge and discharge resistances of the LiFePO4 battery cell can change from $1m\Omega$ to almost $3m\Omega$ at different SOC and temperature. In [41], the ohmic and polarisation resistances of nickel manganese cobalt oxide (NMC) cells are given by the experiment using electrochemical impedance spectroscopy. The ohmic resistance can vary from 0.6 mΩ to 3.5 mΩ at different SOC, temperature and health conditions. Therefore, it is reasonable to assume that without online estimation R'_B and R'_{UC} can be 50%, 150% and 200% of the true internal resistances (R_B and R_{UC}), respectively, in worst case scenarios. According this assumption, the cost function becomes $J = \sum_{k=t}^{t+N} (N_B R'_B I_B^2(k) + N_{UC} R_{UC} I_{UC}^2(k))$ or $J = \sum_{k=t}^{t+N} (N_B R_B I_B^2(k) + N_{UC} R'_{UC} I_{UC}^2(k))$, respectively. The simulation results are presented in Table 4. The difference in HESS losses is used as the performance matric, which is evaluated by Eq. (20). As shown in Table 4, the results obtained using the analytical estimation presented in Section 5.1 show a relative difference of less than 7.61% and an absolute difference of less than 0.38% as compared to the simulation results. The absolute

Table 4
HESS Loss Difference of a 12 s investigation duration under load fluctuations at SS2.

Load	Uncertainty	Case 1	Eq. (21)	$Diff_{abs}$	$Diff_{rlt}$	Case 2	Eq. (21)	$Diff_{abs}$	$Diff_{rlt}$
$P_{FL_{SS2}}$	$50\%R_B$	11.73%	12.10%	0.37%	3.06%	7.34%	7.43%	0.09%	1.21%
$P_{FL_{SS2}}$	$150\%R_B$	2.76%	2.55%	0.21%	7.61%	1.14%	1.07%	0.07%	6.14%
$P_{FL_{SS2}}$	$200\%R_B$	6.70%	6.32%	0.38%	5.67%	2.61%	2.49%	0.12%	4.60%
$P_{FL_{SS2}}$	$50\%R_{UC}$	6.27%	6.32%	0.05%	0.79%	2.46%	2.49%	0.03%	1.20%
$P_{FL_{SS2}}$	$150\%R_{UC}$	3.91%	3.76%	0.15%	3.84%	2.14%	2.04%	0.10%	4.67%
$P_{FL_{SS2}}$	$200\%R_{UC}$	12.41%	12.10%	0.31%	2.50%	7.66%	7.43%	0.23%	3.00%

difference between two results is defined as $Diff_{abs} = |A - B|$, and the relative difference is defined as $Diff_{rlt} = \frac{|A-B|}{A} \times 100\%$, where A and B represent two results. Because "A" and "B" are expressed by percentage in this study, the absolute difference is also shown by percentage.

Several important observations are summarized in the following:

Remark 5.2 (No tracking error formulation in Eq. (22)): In this formulation, the assumptions in Section 5.1 are almost achieved. The impact of the SOC reference term is also ignored. As shown in Table 4, the results from the detailed simulation (columns 3 and 5) are very close to the results from Eq. (21) (columns 4 and 6). The voltage ratio ν and the internal resistance ratio α determine the difference in HESS loss. Note that if the internal resistance used in the MPC is higher than its actual value, the HESS-losses difference will be slightly higher than the estimated value of Eq. (21), and vice versa. For example (highlighted in blue), the internal resistance ratios of $R'_B = 200\%R_B$ and $R'_{UC} = 50\%R_{UC}$ are the same, but the HESS-losses difference of $R'_B = 200\%R_B$ is slightly larger than the value from Eq. (21), while the difference of $R'_{UC} = 50\%R_{UC}$ is slightly smaller. The same phenomenon can be found between $R'_B = 50\%R_B$ and $R'_{UC} = 200\%R_{UC}$ (highlighted in red). The reason is that the tracking error still exists when the HESS parameters are not correct. Larger current is caused by the larger incorrect internal resistance, and vice versa. Furthermore, another case study is performed to evaluate the impact of the load power. The load power is reduced to $50\%P_{FL-SS2}$, which guarantees no constraint is active. As shown in Table 5, even though the load power becomes 50%, the analytical estimation only has a relative difference of less than 2.67% and a absolute difference of less than 0.13% as compared to the simulation results.

Remark 5.3 (Nominal formulation in Eq. (10) within 12 s): In this case study, the trade-off between the tracking error and HESS losses is considered in the nominal formulation in Eq. (10)). The investigation time is chosen as 12 s, which minimizes the impact of the SOC reference term. As shown in Fig. 6, the Pareto fronts show the tradeoff between the tracking error and HESS losses for both Case 1 and 2 at sea state 2, and the result is consistent with that in Table 4. In order to compare the HESS losses difference using Eq. (20), the Pareto fronts are fitted by a first-order polynomial function, and the performance comparison results are shown in Fig. 7. These results demonstrate that the analysis in Section 5.1 is also suitable when the load fluctuations are not fully compensated by HESS.

Remark 5.4 (Nominal formulation in Eq. (10) within 600 s): In this case study, the investigation time is extended to 600 s, which includes the impact of the SOC reference term. To compare with the performance of a 12-s investigation time, the Pareto fronts of 600-s investigation time are shown in Figs. 8 and 9. The SOC reference term requires the battery to keep the UC working in its high-efficiency range, which makes the overcompensated error worse. Compared to the voltage ratio ν and the internal resistance ratio α, the impact of the SOC reference term is not significant, and therefore the analysis in Section 5.1 can still provide insights into how sensitive the HESS to the parameter uncertainty.

5.2.2. Sea states 4 and 6: inequality constraints are active

Sea state 4 is the nominal sea state, which represents a moderate sea condition. At sea state 4, only the UC will operate at its constraints over a short period of time. On the other hand, sea state 6 represents a severe sea condition, in which the propeller will be in-and-out of the water. At sea state 6, both UC and battery will operate at their constraints over a long period of time. This case study provides insights into that how the constraints affect the performance when HESS parameter uncertainties existing. The key observations are summarized in the following Remarks.

Remark 5.5 (Inequality constraints are active over a short period of time): As shown in Fig. 10, the analysis in Section 5.1 is still valid, and the voltage ratio ν and the internal resistance ratio α are still the major factors to determine how sensitive the HESS to its parameter uncertainties. The HESS losses difference using Eq. (20) is shown in Fig. 11, where a first-order polynomial function is used to fit the results in Fig. 10. As one can see, the result in Fig. 11 is similar to that in Fig. 9. The case study demonstrates that the impact of constraints is related to its active time.

Remark 5.6 (Inequality constraints are active over a long period of time): As discussed in Remark 5.5, the active time of constraints is a key factor. At sea state 6, the constraints are active over a long period of time. As shown in Fig. 12, the performance is insensitive to HESS parameter uncertainties. The parameter uncertainties mainly affect the tradeoff between the tracking error and HESS losses, which is equivalent to changing the weighting factors. The desired operation cannot be achieved as parameter uncertainties exist. Note that the uncertainties at SS2 and SS4 also affect the tradeoff, but not as significant as at SS6.

To summarize the key findings, the analysis in Section 5.1 can provide how sensitive the MPC performance is to HESS parameter uncertainties when the constraints are inactive or active over a short period of time. The voltage ratio ν and the internal resistance ratio α are the main factors to determine the sensitivity. As the constraints are

Table 5
HESS Loss Difference of a 12 s investigation duration under 50% load fluctuations at SS2.

Load	Uncertainty	Case 1	Eq. (21)	$Diff_{abs}$	$Diff_{rlt}$	Case 2	Eq. (21)	$Diff_{abs}$	$Diff_{rlt}$
$50\%P_{FL_{SS2}}$	$50\%R_B$	11.96%	12.10%	0.14%	1.16%	7.38%	7.43%	0.05%	0.67%
$50\%P_{FL_{SS2}}$	$150\%R_B$	2.62%	2.55%	0.07%	2.67%	1.08%	1.07%	0.01%	0.93%
$50\%P_{FL_{SS2}}$	$200\%R_B$	6.45%	6.32%	0.13%	2.02%	2.54%	2.49%	0.05%	1.97%
$50\%P_{FL_{SS2}}$	$50\%R_{UC}$	6.35%	6.32%	0.03%	0.47%	2.50%	2.49%	0.01%	0.40%
$50\%P_{FL_{SS2}}$	$150\%R_{UC}$	3.77%	3.76%	0.01%	0.27%	2.04%	2.04%	0.00%	0.00%
$50\%P_{FL_{SS2}}$	$200\%R_{UC}$	12.13%	12.10%	0.03%	0.25%	7.46%	7.43%	0.03%	0.40%

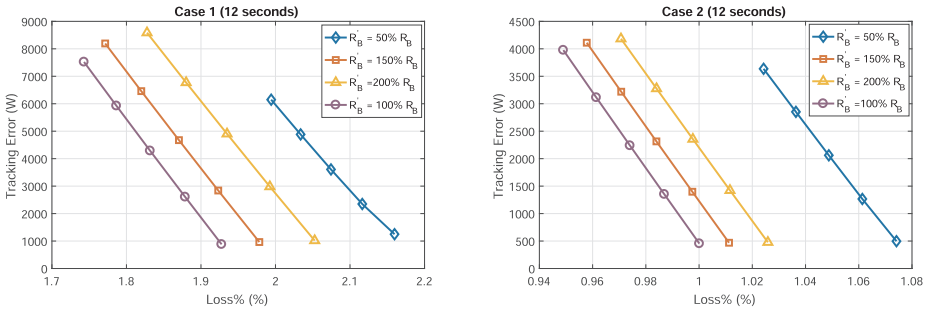

Fig. 6. MPC Results (12 s): Tracking error vs Loss% for both Case 1 and 2 at sea state 2.

active over a long time, the system is insensitive to the parameter uncertainties. However, the MPC performance can be affected in terms of the tradeoff between load fluctuations mitigation and HESS losses minimization. This sensitivity analysis not only demonstrates the importance of the proposed adaptive MPC, but also provide an analytical estimation to quantitatively understand the impact of HESS parameter uncertainties. As shown in Table 4, the impacts of $R_B' = 200\%R_B$ at Case 1 and Case 2 are significantly different. The impact is only 2.46% at Case 2, but becomes 6.70% at Case 1. Furthermore, the same 50% uncertainties (e.g., $R_B' = 150\%R_B$ and $R_B' = 50\%R_B$) could result in significantly different performance (one impact is 2.76% vs. the other is 11.73%). Therefore, this sensitivity analysis could be important in the design phase.

6. Experimental validation and discussion

In order to validate the proposed adaptive MPC and the sensitivity analysis, an experiment has been performed in a scaled test-bed. This test-bed consists of power electronic converters, a load resistance bank, battery and UC modules, and a central micro-controller (Speedgoat). The Speedgoat has an "Intel Core i5-680 3.6 GHz" processor with a 320 GB SATA hard disk main drive and a 4096 MB DDR3 memory. The power electronic converters, which are controlled by the central micro-controller, serve as actuators in controlling the power flow from and to different components in the testbed. The load resistance bank is used to emulate the load fluctuations.

Four Lithium-Iron-Phosphate battery modules are developed for this experimental validation, and each module consists of 12 cells in series. The nominal voltage and capacity are 38.4 V and 100 Ahr, respectively. The entire battery pack provides a nominal voltage up to 154 V. Two ultra-capacitor modules, made by Maxwell Technologies® with 63 farad, are used in this experiment. In this experiment, two UC modules are connected in series, and the reference voltage of the UC pack is defined as 145 V.

6.1. Overview of energy storage controller and optimization solver

In this study, sliding mode control [42] is used for HESS control. The control law is presented as follows:

$$\begin{bmatrix} D_B \\ D_{UC} \end{bmatrix} = \begin{bmatrix} 1 - \frac{V_B}{V_{Bus}} + I_B \frac{R_{L1}+R_{on2}}{V_{Bus}} + K_B \frac{L_B}{V_{Bus}} \left(I_{B,ref} - I_B \right) + \varepsilon_B \frac{L_1}{V_{Bus}} sat \left(I_{B,ref} - I_B \right) \\ 1 - \frac{V_{UC}}{V_{Bus}} + I_{UC} \frac{R_{L2}+R_{on4}}{V_{Bus}} + K_{UC} \frac{L_{UC}}{V_{Bus}} \left(I_{UC,ref} - I_{UC} \right) + \varepsilon_{UC} \frac{L_2}{V_{Bus}} sat \left(I_{UC,ref} - I_{UC} \right) \end{bmatrix}, \quad (24)$$

where V_{Bus} is the DC bus voltage, L_B, and L_{UC} are the inductors of the DC/DC converter for the battery and UC, respectively; R_{L1} and R_{L2} are the resistances corresponding to L_1, and L_2, respectively; D_B and D_{UC} are the duty cycle commands to the DC/DC converters for the battery and UC, respectively, and $K_{B,UC}$ and $\varepsilon_{B,UC}$ are the control gains.

The integrated perturbation analysis and sequential quadratic programming (IPA-SQP) algorithm is used to solve the optimization problem in this study. IPA-SQP approximates the optimal solution numerically using a prediction and correction combination. Neighboring extremal (NE) updates the optimal solution in the prediction step, and SQP corrects the solution if the solution from NE is larger than the tolerance [24].

6.2. Overview of experimental setup

The diagram of the experimental setup is shown in Fig. 13, where the desired DC bus voltage is defined as 200 V and the desired reference voltage of UC is 146 V [33]. The physical constraints, namely maximum and minimum currents of both battery and UC, are 30A and −30A, respectively. The AC power from the gird is converted to DC power by a three-phase diode rectifier, and a DC/DC converter (PCM1) is used to "buck" the DC voltage down to the nominal voltage. Load fluctuations are generated by the resistive load bank, which is controlled by a DC/

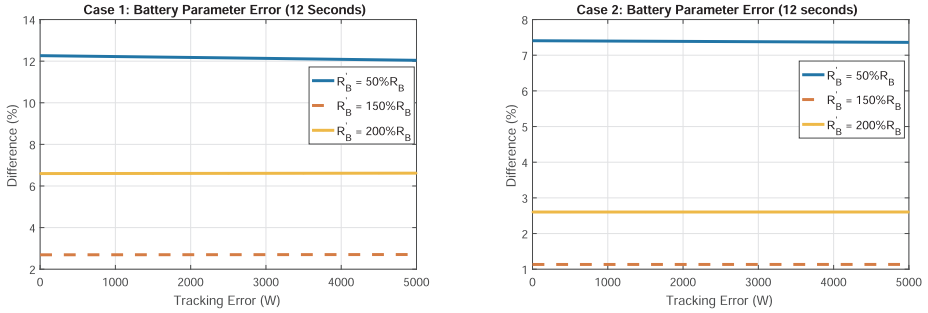

Fig. 7. Data Fitting Results (12 s): Difference (%) vs Tracking error for both Case 1 and 2 at sea state 2.

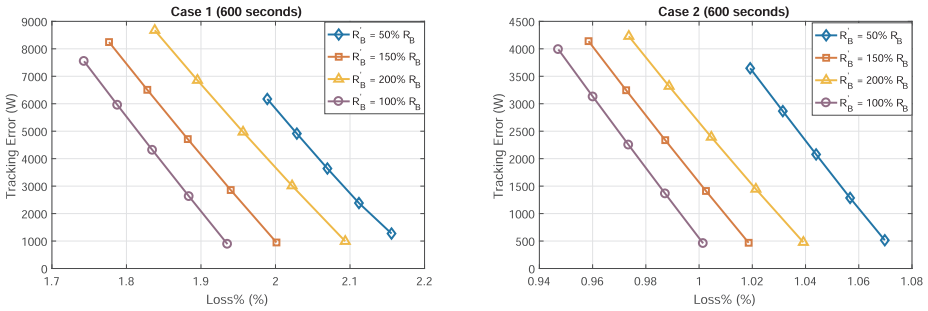

Fig. 8. MPC Results (600 s): Tracking error vs Loss% for both Case1 and 2 at sea state 2.

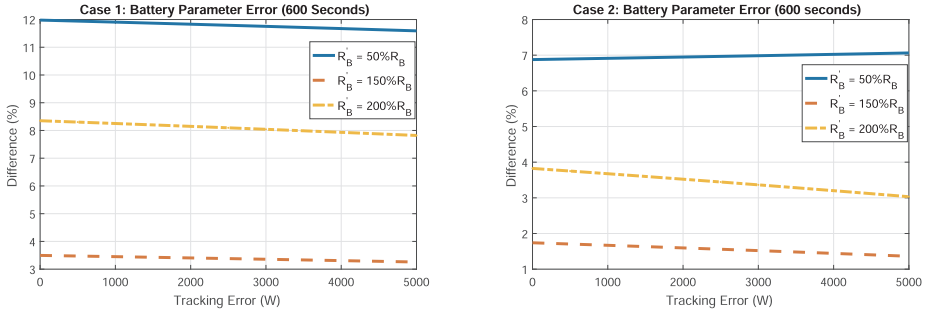

Fig. 9. Data Fitting Results (600 s): Difference (%) vs Tracking error for both Case1 and 2 at sea state 2.

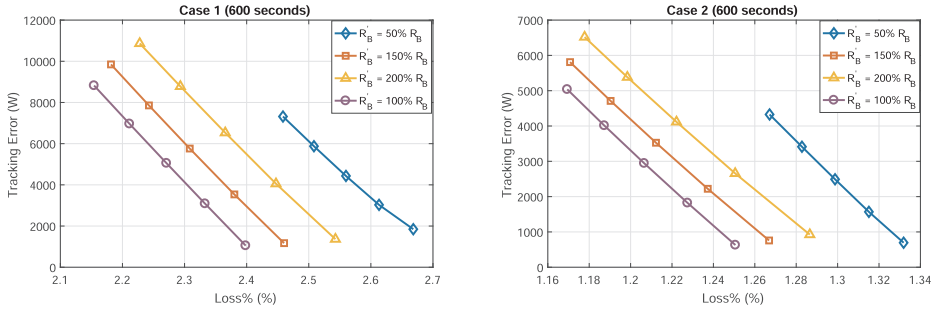

Fig. 10. MPC Results: Tracking error vs Loss% for both Case1 and 2 at sea state 4.

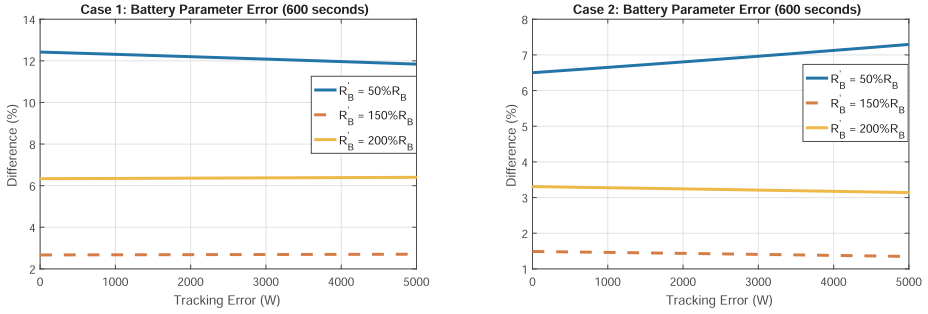

Fig. 11. Data Fitting Results: Difference (%) vs Tracking error for both Case1 and 2 at sea state 4.

DC converter (PCM5). However, the resistive load bank can only absorb power so that a DC/DC converter (PCM2) is controlled to provide the average power to the DC bus. In this way, the load fluctuations can be emulated in this experiment, and they are scaled to a peak value of 2 kW for both sea states 4 and 6. The schematic of the adaptive MPC is shown in Fig. 14, where the predictive horizon N is chosen to be 20 and the sampling time of the adaptive MPC is 0.01 s.

6.3. Experimental results and discussion

In the adaptive MPC, the recursive least square with forgetting factor is used for the parameter identification. The parameter identification results of the battery and UC are shown in Fig. 15 and 16, and all parameters can converge to relatively stable values. The equivalent series internal resistance R_B is about $64m\Omega$, and the OCV changes via time. The terminal voltage is estimated based on the identified V_{OC} and R_B, and it shows that the estimated battery terminal voltage can track the measured voltage. The capacity of UC is 31.5 F (the nominal capacity of the UC pack is also 31.5 F) and its equivalent series internal resistance R_{UC} is about 18 mΩ. The estimation errors of battery and UC are both below 0.5%, which means a satisfactory identification performance.

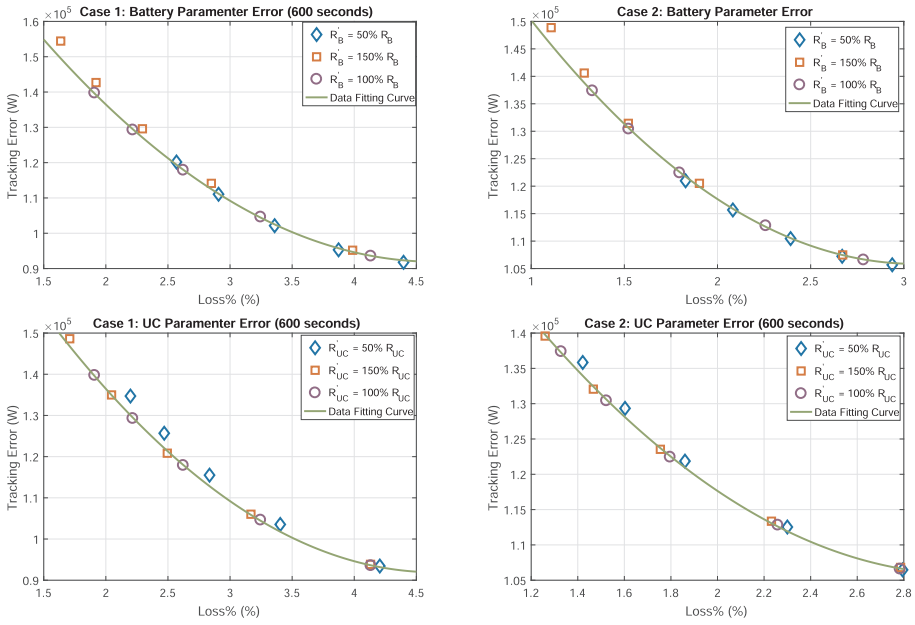

Fig. 12. MPC Results: Tracking error vs Loss% for both Case 1 and 2 at sea state 6.

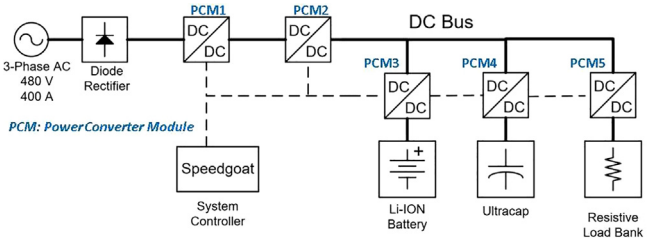

Fig. 13. Diagram of real-time MPC experiment.

In order to evaluate the performance of the adaptive MPC, a comparison study is performed at both SS4 and SS6. The adaptive MPC is implemented in the first case, and in the other two cases the MPC without online parameter identification is considered. The battery internal resistance used in these two cases are assumed to be $R_B' = 50\%R_B$ and $R_B' = 200\%R_B$, and the incorrect values could be caused by the temperature variation and the battery life degradation.

The experimental results are shown in Figs. 17 and 18. The experimental results and analysis results from Eq. (21) are summarized in Table 6, where the performance matric in Eq. (20) is used to evaluate the results. The experimental results demonstrate the effectiveness of the proposed adaptive MPC as well as the sensitivity analysis. Without the online parameter identification, the HESS losses could increase by almost 15%. Furthermore, the sensitivity analysis results are close to the experimental results at both SS4 and SS6. Although the load fluctuations are different for SS4 and SS6 in this experiment, the results are almost the same because the constraints are inactive. As the voltage ratio ν and the internal resistance ratio α are design parameters, this sensitivity analysis can play an important role in the design phase.

7. Conclusion

The parameter uncertainty of HESS can significantly affect system performance. In order to address this issue, an adaptive model predictive control, which combines online parameter identification with MPC, is developed in this paper. The online parameter identification can effectively capture the parameter variations, and the model predictive control optimally splits the power between the battery and UC, and deals with the constraints. In order to provide insights into how sensitive the performance to the parameter uncertainties, a sensitivity analysis is studied to identify the major impact factors. Both simulation and experiment are performed to show the effectiveness of the proposed method in all-electric ship energy management to mitigate load fluctuations and improve system efficiency and reliability. Compared to model predictive control without the online parameter identification,

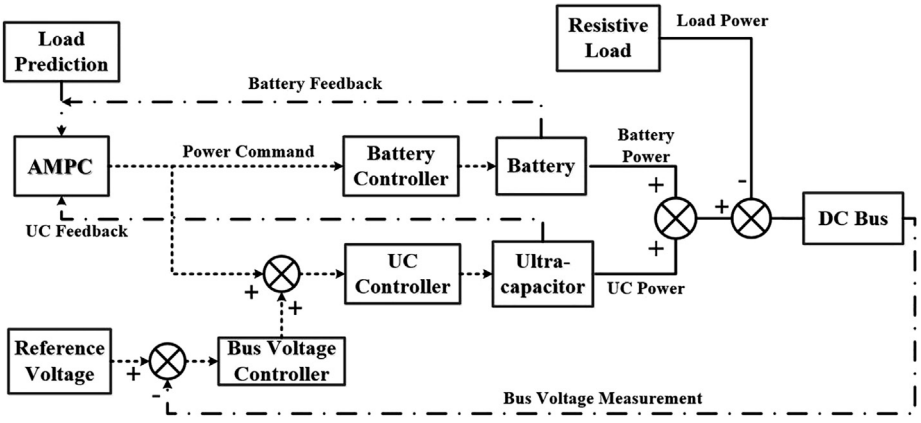

Fig. 14. Schematic of the real-time adaptive MPC.

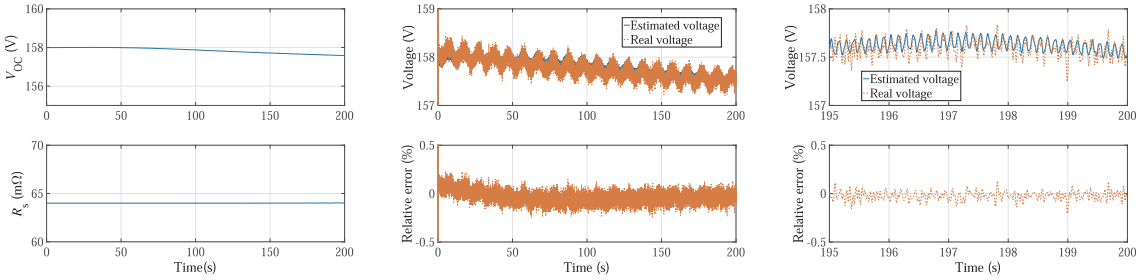

Fig. 15. Parameter identification results of battery at SS4: identified values, terminal voltage error, and zoomed-in plot.

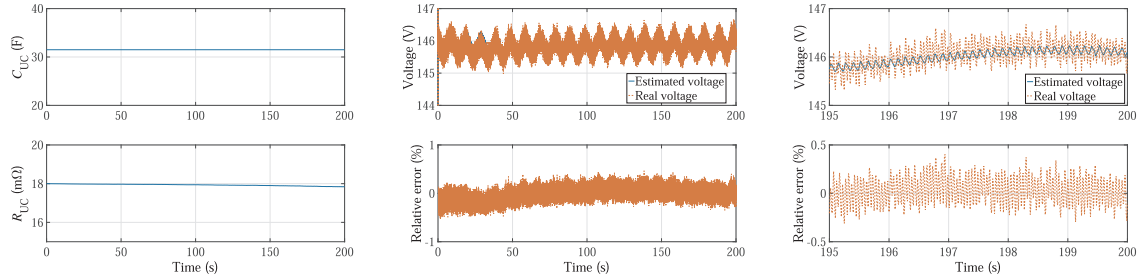

Fig. 16. Parameter identification results of UC at SS4: identified values, terminal voltage error, and zoomed-in plot.

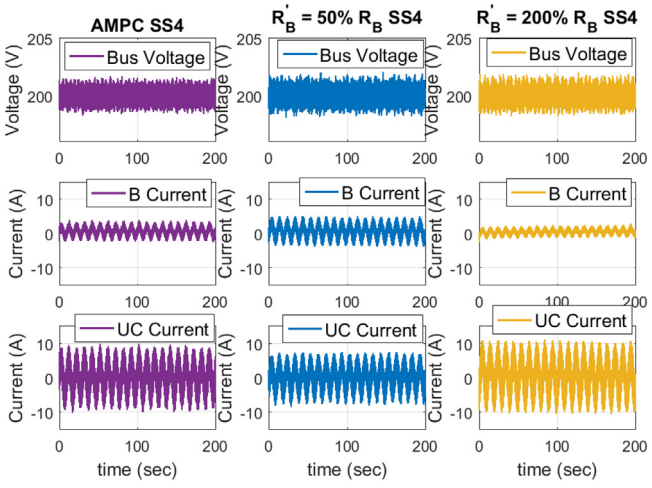

Fig. 17. Experimental results of scaled SS4 load fluctuations.

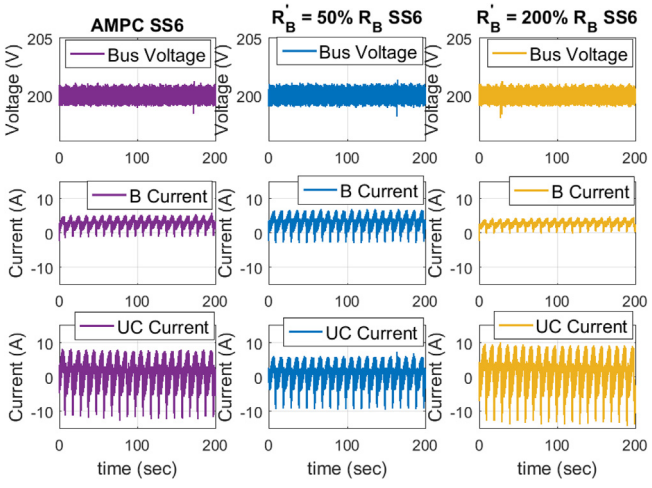

Fig. 18. Experimental results of scaled SS6 load fluctuations.

Table 6
Experimental validation using SS4 and SS6 profile.

Parameter uncertainty	Experimental results (SS4)	Experimental results (SS6)	Results (Equ. (21))
$R_B' = 50\%R_B$	13.8448%	14.5299%	11.9066%
$R_B' = 200\%R_B$	6.5716%	6.4175%	5.9600%

the improvement on HESS losses can be as high as 15% in the experiment. The proposed adaptive MPC could also be used in other applications, such as hybrid electric vehicles and renewable energy, to deal with the parameter uncertainties and optimize the system performance.

Declaration of Competing Interest

The authors declare that they have no known competing financial interests or personal relationships that could have appeared to influence the work reported in this paper.

Acknowledgment

This material is based upon work supported by the U.S. Office of Naval Research (ONR) under Grant N00014-16-1-3108 and N00014-15-1-2668.

References

[1] Hemmati R, Saboori H. Emergence of hybrid energy storage systems in renewable energy and transport applications–a review. Renew Sustain Energy Rev 2016;65:11–23.
[2] Hu Z, Xu L, Li J, Ouyang M, Song Z, Huang H. A reconstructed fuel cell life-prediction model for a fuel cell hybrid city bus. Energy Convers Manage 2018;156:723–32.
[3] Ahmadi S, Bathaee S, Hosseinpour AH. Improving fuel economy and performance of a fuel-cell hybrid electric vehicle (fuel-cell, battery, and ultra-capacitor) using optimized energy management strategy. Energy Convers Manage 2018;160:74–84.
[4] Choudar A, Boukhetala D, Barkat S, Brucker JM. A local energy management of a hybrid PV-storage based distributed generation for microgrids. Energy Convers Manage 2015;90:21–33.
[5] Pavković D, Lobrović M, Hrgetić M, Komljenović A. A design of cascade control system and adaptive load compensator for battery/ultracapacitor hybrid energy storage-based direct current microgrid. Energy Convers Manage 2016;114:154–67.

[6] Wang B, Xu J, Xu D, Yan Z. Implementation of an estimator-based adaptive sliding mode control strategy for a boost converter based battery/supercapacitor hybrid energy storage system in electric vehicles. Energy Convers Manage 2017;151:562–72.
[7] Zhang WB, Wenbin, Li JQ, Xu LF, Ouyang MG. Optimization for a fuel cell/battery/capacity tram with equivalent consumption minimization strategy. Energy Convers Manage 2017;134:59–69.
[8] Hou J, Sun J, Hofmann HF. Control development and performance evaluation for battery/flywheel hybrid energy storage solutions to mitigate load fluctuations in all-electric ship propulsion systems. Appl Energy 2018;212:919–30.
[9] Yan D, Lu L, Li Z, Feng X, Ouyang M, Jiang F. Durability comparison of four different types of high-power batteries in HEV and their degradation mechanism analysis. Appl Energy 2016;179:1123–30.
[10] Zou CF, Zhang L, Hu XS, Wang ZP, Wik T, Pecht M. A review of fractional-order techniques applied to lithium-ion batteries, lead-acid batteries, and supercapacitors. J Power Sources 2018;390:286–96.
[11] Liu HQ, Wei ZB, He WD, Zhao JY. Thermal issues about Li-ion batteries and recent progress in battery thermal management systems: a review. Energy Convers Manage 2017;150:304–30.
[12] http://www.maxwell.com/products/ultracapacitors/125v-tran-modules.
[13] Hou J, Sun J, Hofmann HF. Adaptive model predictive control with propulsion load estimation and prediction for all-electric ship energy management. Energy 2018;150:877–99.
[14] Zhang L, Hu XS, Wang ZP, Sun FC, Dorrell DG. A review of supercapacitor modeling, estimation, and applications: a control/management perspective. Renew Sustain Energy Rev 2018;81:1868–78.
[15] Kwak Y, Huh JH. Development of a method of real-time building energy simulation for efficient predictive control. Energy Convers Manage 2016;133:220–9.
[16] Rodrigues E, Godina R, Pouresmaeil E, Ferreira JR, Catalão J. Domestic appliances energy optimization with model predictive control. Energy Convers Manage 2017;142:402–13.
[17] Li L, Zhang YB, Yang C, J Yan B, Martinez CM. Model predictive control-based efficient energy recovery control strategy for regenerative braking system of hybrid electric bus. Energy Convers Manage 2016;111:299–314.
[18] Zhang S, Xiong R, Sun F. Model predictive control for power management in a plug-in hybrid electric vehicle with a hybrid energy storage system. Appl Energy 2017;185:1654–62.
[19] Dufo-López R, Fernández-Jiménez LA, Ramírez-Rosado IJ, Artal-Sevil JS, Domínguez-Navarro JA, Bernal-Agustín JL. Daily operation optimisation of hybrid stand-alone system by model predictive control considering ageing model. Energy Convers Manage 2017;134:167–77.
[20] Mayne DQ. Model predictive control: recent developments and future promise. Automatica 2014;50(12):2967–86.
[21] Doerry N, Amy J, Krolick C. History and the status of electric ship propulsion, integrated power systems, and future trends in the us navy. Proc IEEE 2015;103(12):2243–51.
[22] Hebner R, Davey K, Herbst J, Hall D, Hahne J, Surls D, Ouroua A. Dynamic load and storage integration. Proc IEEE 2015;103(12):2344–54.
[23] Geertsma RD, Negenborn RR, Visser K, Hopman JJ. Design and control of hybrid power and propulsion systems for smart ships: a review of development. Appl Energy 2017;194:30–54.
[24] Park H, Sun J, Pekarek S, Stone P, Opila D, Meyer R, Kolmanovsky I, DeCarlo R. Real-time model predictive control for shipboard power management using the IPA-SQP approach. IEEE Trans Control Syst Technol 2015;23(6):2129–43.
[25] Bø TI, Johansen TA. Battery power smoothing control in a marine electric power plant using nonlinear model predictive control. IEEE Trans Control Syst Technol 2017;25(4):1449–56.
[26] Bø TI, Johansen TA. Dynamic safety constraints by scenario-Based economic model predictive control of marine electric power plants. IEEE Trans Transp Electrif 2017;3(1):13–21.
[27] Van Vu, Tuyen David Gonsoulin, Diaz Fernand, Edrington Chris S, El-Mezyani Touria. Predictive control for energy management in ship power systems under high-power ramp rate loads. IEEE Trans Energy Convers 2017;32(2):788–97.
[28] Skjong Espen, Are Suul Jon, Rygg Atle, Johansen Tor Arne, Molinas Marta. System-wide harmonic mitigation in a diesel-electric ship by model predictive control. IEEE Trans Ind Electron 2016;63(7):4008–19.
[29] Haseltalab Ali, Negenborn Rudy R. Model predictive maneuvering control and energy management for all-electric autonomous ships. Appl Energy 2019;251:113308.
[30] Wang Kai, Yan Xinping, Yuan Yupeng, Jiang Xiaoli, Lin Xiao, Negenborn Rudy R. Dynamic optimization of ship energy efficiency considering time-varying environmental factors. Transp Res Part D: Transport Environ 2018;62:685–98.
[31] Hannan MA, Lipu M, Hussain A, Mohamed A. A review of lithium-ion battery state of charge estimation and management system in electric vehicle applications: challenges and recommendations. Renew Sustain Energy Rev 2017;78:834–54.
[32] Hou J, Sun J, Hofmann HF. Mitigating power fluctuations in electric ship propulsion with hybrid energy storage system: design and analysis. IEEE J Oceanic Eng 2018;43(1):93–107.
[33] Hou J, Song Z, Park H, Hofmann H, Sun J. Implementation and evaluation of real-time model predictive control for load fluctuations mitigation in all-electric ship propulsion systems. Appl Energy 2018;230:62–77.
[34] Hu X, Li S, Peng H. A comparative study of equivalent circuit models for Li-ion batteries. J Power Sources 2012;198:359–67.
[35] Song Z, Hou J, Hofmann H, Lin X, Sun J. Parameter identification and maximum power estimation of battery/supercapacitor hybrid energy storage system based on cramer-rao bound analysis. IEEE Trans Power Electron 2019;34(5):4831–43.
[36] Hu X, Xiong R, Egardt B. Model-based dynamic power assessment of lithium-ion batteries considering different operating conditions. IEEE Trans Ind Inf 2014;10(3):1948–59.
[37] Sun F, Xiong R, He H. Estimation of state-of-charge and state-of-power capability of lithium-ion battery considering varying health conditions. J Power Sources 2014;259:166–76.
[38] Song Z, Wu X, Li X, Sun J, Hofmann H, Hou J. Current profile optimization for combined state of charge and state of health estimation of lithium ion battery based on cramer-rao bound analysis. IEEE Trans Power Electron 2019;34(7):7067–78.
[39] Zou Y, Hu X, Ma H, Li S. Combined state of charge and state of health estimation over lithium-ion battery cell cycle lifespan for electric vehicles. J Power Sources 2015;273:793–803.
[40] Song Ziyou, Hofmann Heath, Li Jianqiu, Hou Jun, Han Xuebing, Ouyang Minggao. Energy management strategies comparison for electric vehicles with hybrid energy storage system. Appl Energy 2014;134:321–31.
[41] Waag Wladislaw, Kabitz Stefan, Uwe Sauer Dirk. Experimental investigation of the lithium-ion battery impedance characteristic at various conditions and aging states and its influence on the application. Appl Energy 2013;102:885–97.
[42] Song Z, Hou J, Hofmann H, Li J, Ouyang M. Sliding-mode and Lyapunov function-based control for battery/supercapacitor hybrid energy storage system used in electric vehicles. Energy 2017;122:601–12.